


Hyperspectral Three-Dimensional Refractive-Index Imaging Using Snapshot Optical Tomography

Yongjin Sung¹**College of Engineering and Applied Science, University of Wisconsin, Milwaukee, Wisconsin 53211, USA* (Received 3 October 2022; revised 16 November 2022; accepted 22 November 2022; published 24 January 2023; corrected 18 April 2023)

The refractive index serves as an intrinsic contrast in light-scattering measurements for the estimation of the size, shape, and heterogeneities of microscopic particles. The refractive index of cells, intracellular organelles, and extracellular materials is an important input to the analysis of diffuse optical imaging of biological tissues. To improve the accuracy, the measurement is often performed at multiple discrete wavelengths or sometimes over a continuous wavelength range. Knowledge of the refractive index as a function of the wavelength is important, as the analysis of the acquired signal heavily relies on the relationship. Digital holographic tomography allows us to directly measure the three-dimensional (3D) refractive-index map of a heterogeneous microscopic specimen. Typically, a multitude of images are recorded for varying angles of illumination and a tomographic reconstruction algorithm is applied for the 3D reconstruction. Hyperspectral 3D refractive-index imaging has been demonstrated by combining the beam-rotation tomography with a wavelength-scanning light source; however, the data acquisition is slow due to the requirement of scanning both the orientation and the wavelength of the illumination. Recently, several strategies have been proposed to acquire the 3D tomogram in a single snapshot. Here, we combine snapshot holographic optical tomography with a wavelength-scanning laser to demonstrate hyperspectral 3D refractive-index imaging at high throughput. Using the developed system, we measure the refractive-index dispersion of polystyrene beads and single living HeLa cells.

DOI: [10.1103/PhysRevApplied.19.014064](https://doi.org/10.1103/PhysRevApplied.19.014064)

I. INTRODUCTION

The refractive index is an important physical property of a material and has served as an intrinsic contrast in the light-scattering measurement of powders, microplastics, synthesized nanoparticles, etc. [1]. In a light-scattering measurement, the refractive index of the interrogated specimens is typically required as an input to estimate the size, shape, and heterogeneities from the measured scattering signal. The refractive index is typically obtained for a bulk material, from which the micro- or nanoparticles are derived. To be more precise, the refractive-index value of the particles needs to be measured, as it can be different from that of a bulk material due to the physical and chemical changes during a manufacturing process. To improve the accuracy, the light-scattering measurement is often performed at multiple wavelengths, which requires the refractive-index values for the selected wavelengths. In addition to being used as an input to the light-scattering measurement, the refractive index has served as an intrinsic contrast for label-free imaging of biological cells and tissues. In cell imaging, the measured refractive index has been related to the density of dry materials in a cell [2] to

study the cell growth [3–5], to study the biomechanics of red blood cells [6,7], to distinguish cancer cells from normal cells [8–10], to discern lineage commitments in stem cells [11], etc. Refractive-index dispersion has been utilized [12] to distinguish white matter from gray matter in a frozen brain-tissue slice [13], to obtain the hemoglobin concentration in homogeneous red blood cells [14], and to quantify nucleic acids and proteins in a living cell [15]. In diffuse optical imaging of a human tissue, the refractive index of cells, intracellular organelles, and extracellular materials (e.g., collagen) is a major input to the analysis. To probe multiple endogenous and exogenous chromophores, diffuse optical imaging has been performed at multiple wavelengths [16] or even for a continuous wavelength range [17]. The refractive-index values for various tissue components need to be known for the selected wavelength range.

Recent developments in digital holographic tomography (DHT), which is also called tomographic phase microscopy, quantitative phase tomography, etc., enable us to measure the three-dimensional (3D) refractive-index map of a heterogeneous microscopic specimen at increasingly higher resolution and accuracy [18,19]. Multispectral 3D refractive-index imaging has been demonstrated using multiple laser outputs [20,21]. Combining

*ysung4@uwm.edu

DHT with a wavelength-scanning source, hyperspectral 3D refractive-index imaging has also been demonstrated [22,23]. For 3D refractive-index imaging, DHT typically records multiple images for varying angles of illumination [24,25], varying orientations of the sample [26], or both [27,28]. Each recorded image is often called a projection image, as in x-ray computed tomography, even though the projection approximation, which assumes that the light passes through the sample rectilinearly without diffraction, is not adopted. Significant progress has been made to reduce the data processing time [29], which promises real-time 3D imaging and visualization [30]. However, the serial acquisition of projection images currently imposes a fundamental limitation on the data collection and thus the final imaging throughput of DHT. The imaging throughput of hyperspectral 3D refractive-index imaging is further limited by the requirement to change the wavelength. Recently, several strategies have been proposed to record the 3D refractive-index map in a single snapshot [31–33]. For example, we have used angular multiplexing and defocused imaging to record 32 projection images in a single snapshot at the cost of reduced spatial resolution [31]. We have called this technique snapshot holographic optical tomography (SHOT). Mirsky *et al.* have used angular multiplexing without defocused imaging to record a relatively small number (12) of projection images at high resolution and yet at low angular sampling [32]. Xiong *et al.* have demonstrated a different approach using the principle of light-field imaging for 3D snapshot refractive-index imaging using partially coherent light [33].

In this study, we demonstrate hyperspectral 3D refractive-index imaging by combining SHOT with a wavelength-scanning laser. Built upon modified Mach-Zehnder interferometry, SHOT requires the optical path lengths (OPLs) of the sample and reference arms to be matched. This task is not trivial, as the sample and reference arms are not identical, which causes the OPLs to change differently with the wavelength, and the coherence length of the wavelength-scanning source is only about 20 μm after the tunable filter. To match the OPLs across all the measured wavelengths, we employ a variable-optical-path-length (VOPL) strategy, using a mirror mounted on a motorized translation stage [23].

II. SNAPSHOT OPTICAL TOMOGRAPHY FOR HYPERSPECTRAL 3D REFRACTIVE-INDEX IMAGING

A. Snapshot holographic optical tomography

SHOT uses a microlens array (MLA) to generate a multitude of collimated beams, each of which is incident onto the sample at a different angle and provides a different perspective of the 3D specimen. On the one hand, this concurrent illumination obviates the need to scan the illumination angle. On the other, all the beams overlapping

at the sample plane will also overlap at the image plane, which renders the projection images inseparable. However, as the beams cross the image plane along different directions, if the camera is placed at a defocused plane, the projection images can be separated, although they will be seriously blurred. It is noteworthy that once both the amplitude and phase of a propagating light field are determined at a plane orthogonal to the direction of propagation, the light fields at any other planes in the propagation path can be calculated using the following angular-spectrum scalar wave theory equation [34]:

$$U_2(x, y) = \mathcal{F}^{-1} \{H_\lambda(u, v; -\Delta z) \mathcal{F} \{U_1(x, y)\}\}, \quad (1)$$

where \mathcal{F} and \mathcal{F}^{-1} are the two-dimensional (2D) Fourier and inverse Fourier transforms, respectively, and λ is the wavelength of the light in free space. The light fields $U_1(x, y)$ and $U_2(x, y)$ are each a function defined as $U(x, y) = A(x, y) \exp(\Phi(x, y))$, where $A(x, y)$ and $\Phi(x, y)$ represent the amplitude and phase distributions, respectively. Δz is the distance between the two planes where $U_1(x, y)$ and $U_2(x, y)$ are defined. (u, v) are the spatial-frequency coordinates corresponding to (x, y) , respectively. $H_\lambda(u, v; z)$ is the transfer function for the free-space propagation over the axial distance of z , defined as $H_\lambda(u, v; z) = \exp \left\{ i2\pi z \sqrt{(1/\lambda)^2 - u^2 - v^2} \right\}$. Propagating the light fields from the camera plane to the image plane, we can retrieve the phase images at the image plane for all the different illumination directions. The 3D refractive-index map of the specimen can be reconstructed from the retrieved phase images, as is typically done in DHT. This single-shot measurement is repeated while varying the wavelength of the illumination light for hyperspectral 3D refractive-index imaging.

Figure 1 shows a schematic diagram of the system, which is built upon SHOT and modified to perform hyperspectral 3D refractive-index imaging. We add a supercontinuum laser (NKT Photonics, WL SC400-4) and a tunable band-pass filter (NKT Photonics, LLTF-VIS) to the original SHOT system, which allows scanning of the wavelength in the (400–1000)-nm range with a bandwidth [full width at half maximum (FWHM)] of 1.0–2.5 nm. A combination of a MLA and relay optics generates 32 beams incident onto the sample plane (SP) with the maximum incident angle of 50° with respect to the optical axis. The beams pass through the sample along different directions and generate projection images (i.e., images of the projected phase) for different illumination directions. We use a $100\times$ objective lens (Olympus, UPlanFl) with a numerical aperture (NA) of 1.3 and the overall imaging magnification factor is 48.6. The effective NA for each subimage is about 0.47; thus, the diffraction limit is $0.67 \mu\text{m}$. The FWHM of the 3D point spread function (PSF), assessed using $1\text{-}\mu\text{m}$ polystyrene beads in water, is measured to

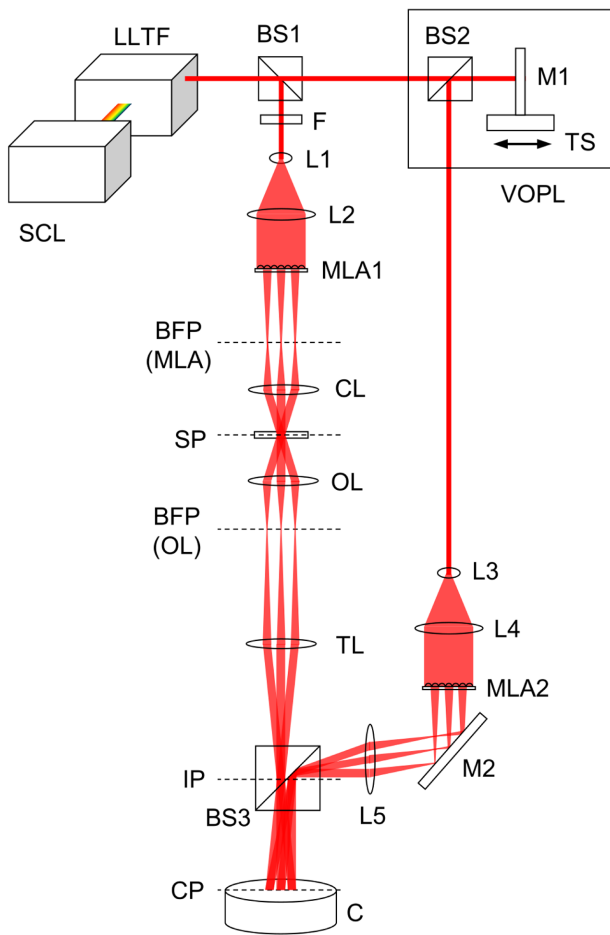


FIG. 1. A schematic diagram of the setup. SCL, supercontinuum laser; LLTF, tunable filter; BS1-BS3, beam splitters; F, neutral density filter; L1-L5, lenses; M1-M2, mirrors; TS, translation stage; MLA1-MLA2, microlens arrays; CL, condenser lens; OL, objective lens; TL, tube lens; C, camera; VOPL, variable optical path length; SP, sample plane; BFP, back-focal plane; IP, image plane; and CP, camera plane.

be $2.0 \mu\text{m}$ in the horizontal direction and $2.8 \mu\text{m}$ along the vertical direction, without subtracting the actual bead size. This resolution degradation from the theoretical limit is mainly attributed to the use of off-axis Fresnel holography. The amplitude and phase, which compose the light field, can be recorded using interferometry [35], a Shack-Hartmann sensor [36], or a transport-of-intensity method [37,38]. Among the various choices, we adopt interferometry, which allows for recording the phase with high accuracy. The quasimonochromatic laser light after the tunable band-pass filter has sufficiently high coherence to generate an interference image with uniform visibility across the entire field of view, when the OPLs of the sample and reference arms are matched. To match the OPLs, we vary the OPL of the reference arm using a mirror mounted on a motorized translation stage (Thorlabs, MTS50-Z8), actuated by a dc servo motor. The exact

positions of the mirror for varying wavelengths are determined by manually inspecting the fringe contrast at 50-nm wavelength steps and then using an interpolation for all the wavelength steps. To record the images, we use a 14-bit charge-coupled device (CCD) camera (Allied Vision, Pike F-421B) with 2048×2048 pixels of $7.4\text{-}\mu\text{m}$ pixel size. We use LabVIEW (National Instruments) for synchronous control of the tunable filter, the motorized stage in the reference arm, and the camera exposure time.

B. Sample preparation and imaging procedure

HeLa cells (ATCC) are maintained at 37°C and 5% CO_2 in Dulbecco's modified Eagle's medium (Fisher Scientific, 11966025) supplemented with 5% (v/v) fetal bovine serum (Fisher Scientific, 10082139) and 1% (v/v) penicillin-streptomycin (Fisher Scientific, 15140122). For imaging, we detach the cells from the surface using TrypLE Express (Fisher Scientific, 12604021), dilute the cell suspension by 100 times with the culture medium, and plate the cells on a sterilized cover slip. After incubating the sample for 24 h, we put another cover slip on the sample and mount it on the microscope stage. In tandem with the hyperspectral SHOT instrument, we install a bright-field microscope with a large field of view, which facilitates identification of the cells to be imaged. To record the bright-field image of a transparent specimen, we use a differential-phase-contrast method with asymmetric illumination [39]. The recorded bright-field image is also used for comparison with the cross sections of the reconstructed tomograms. The wavelength is scanned in the range of 530–670 nm at 5-nm step size. For wavelengths below 530 nm and above 670 nm, the raw interferogram images have poor fringe visibility, presumably due to low transmission efficiency and chromatic aberration of the optical components. Before taking the cell images, we find an empty region and record a set of background images for the same wavelength range and step size. These background images are used in postprocessing to subtract the residual background phase in the sample images. The tunable filter has a stabilization time of about 65 ms for the wavelength scan at 5-nm steps, while the camera frame rate is about 7 frames/s for the acquisition of 14-bit images at full resolution. The data acquisition speed is limited by the settling time of the motorized translation stage, which is installed for the VOPL strategy. Without optimization, it takes 41 s to acquire 29 images for each sample. The experiment is completed within 1 h of preparing the sample. The experimental protocol is approved by the Institutional Biosafety Committee at the University of Wisconsin-Milwaukee.

C. Image processing and tomographic reconstruction

Figure 2 shows the SHOT image processing steps. SHOT records a series of images at a defocused camera plane while scanning the wavelength of illumination. The

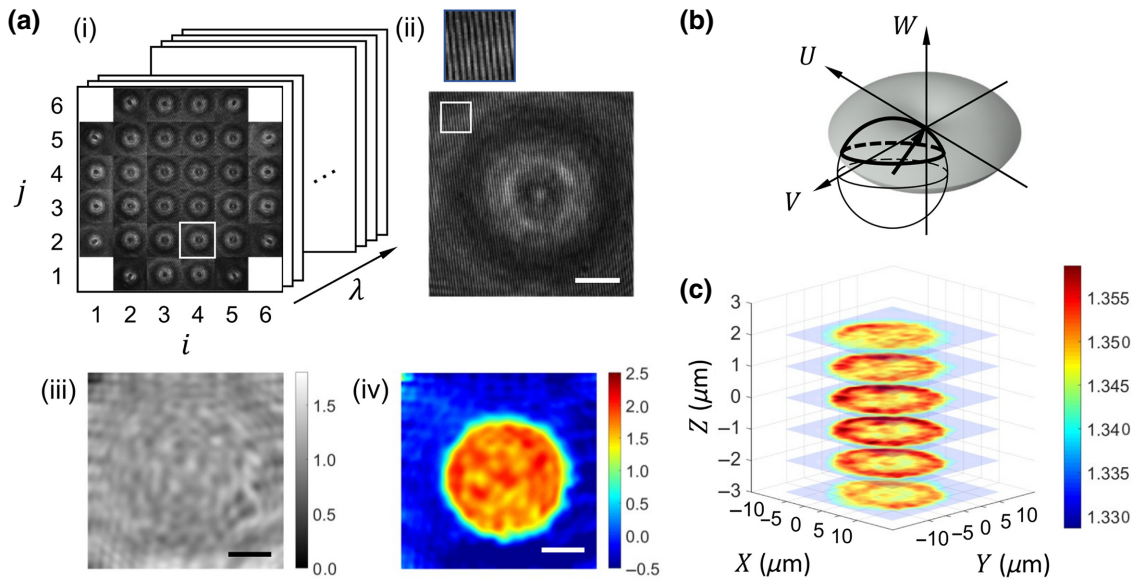


FIG. 2. The data processing steps. (a) (i) A raw-image stack acquired with SHOT for varying wavelengths, which shows an example raw image at the 630-nm wavelength for a living HeLa cell in culture medium. For each wavelength, the raw image comprises a multitude of subimages. Each subimage records a defocused light field as an interferogram for the illumination beam that is generated by one of the lenslets in the MLA. As an example, one of the subimages, marked as a square in (i), is magnified and shown in (ii). A small region in the background is further magnified and illustrated at the top, showing interference fringes with the period of about 3 pixels. (iii),(iv) The amplitude and phase images, respectively, at the image plane, which are calculated from the subimage shown in (ii). Scale bar $10 \mu\text{m}$. (b) The light field synthesized from the amplitude (iii) and phase (iv) images in (a) is mapped onto the Ewald's sphere (hemispherical cap) in the 3D spatial frequency space. The thick arrow, drawn from the center of the sphere to the origin of the coordinates, represents the wave vector (u_0, v_0, w_0) for the incident plane wave that generates the recorded light field, i.e., the amplitude (iii) and phase (iv) images in (a). Other subimages are mapped onto the Ewald's spheres shifted from the origin of the coordinates by different amounts. The shaded volume of a donut shape represents the 3D spatial frequency map that can be obtained after completing the mapping. (c) Horizontal cross sections of the 3D refractive-index map of a HeLa cell, which is reconstructed from the raw image shown in (a). The interval between the cross sections is $1 \mu\text{m}$.

raw image for each wavelength is an interferogram and comprises a multitude of subimages, which correspond to different illumination angles. For each subimage, both the amplitude and phase, which compose the light field, can be extracted from the interferogram using Fourier analysis [35]. The retrieved amplitude and phase images are out of focus; however, through applying angular-spectrum scalar wave theory [Eq. (1)], sharp amplitude and phase images at the image plane can be obtained. Figure 2(a) shows an example raw image of a HeLa cell in culture medium for a 630-nm wavelength, where i and j are the indices for the horizontal and vertical positions, respectively, of each subimage. One of the subimages ($i = 4, j = 2$) is magnified on the right. It is noteworthy that the subimages have the same fringe orientation, because the reference beams are shifted replicas of the sample beams; the difference in the propagation angles of each sample beam and the corresponding reference beam is the same for all the subimages. The amplitude and phase images extracted from each subimage are used to synthesize the light field, which is propagated to the image plane using Eq. (1). From the propagated light field, the amplitude and phase images

at the image plane can be retrieved and are shown in Figs. 2(a)(iii) and 2(a)(iv), respectively. The other subimages can be similarly processed to generate the amplitude and phase images at the image plane for 32 illumination angles. Note that each subimage is propagated from the camera plane to the image plane along a different direction, which is given by the wave vector of the incident plane wave at the image plane. The 3D refractive-index map can be synthesized from the 32 phase images, as is typically done in DHT and described below.

The theoretical basis of the tomographic reconstruction in DHT and SHOT is that, for plane-wave illumination, the scattered light field after a specimen can be related to the refractive index of the specimen in the spatial-frequency space or the Fourier space [40]. Suppose that a plane wave of wavelength λ is incident onto a sample immersed in a medium of the refractive index n_0 . The wave vector of the incident plane wave can be represented by (u_0, v_0, w_0) , where $w_0 = \sqrt{(n_0/\lambda)^2 - u_0^2 - v_0^2}$, and the light field in the sample space can be written as $U^{(l)}(x, y, z) = \exp\{i2\pi(u_0x + v_0y + w_0z)\}$. Note that u_0 and v_0 uniquely determine w_0 . Here, we assume that the

scattered light field is measured at the image plane, which is conjugate to the sample plane ($z = 0$). The light field at $z = 0$ due to the incident plane wave is hereafter written as $U^{(I)}(x, y; u_0, v_0)$. The scattering potential of the sample is defined in terms of the refractive index $n(x, y, z)$ as $V(x, y, z) = -(2\pi/\lambda_0)^2(n(x, y, z)^2 - n_0^2)$ [40]. For a plane wave with wave vector (u_0, v_0, w_0) , the scattered light field $U^{(S)}(x, y; u_0, v_0)$ can be simply related to the scattering potential $V(x, y, z)$ of the sample under the first-order Born or Rytov approximation [41]. Both approximations produce the same relationship, shown in the following equation for different definitions of $U^{(S)}(x, y; u_0, v_0)$:

$$\mathcal{F}\{U^{(S)}(x, y; u_0, v_0)\} = \frac{\pi}{iw} \tilde{V}(u - u_0, v - v_0, w - w_0), \quad (2)$$

where \mathcal{F} is the 2D Fourier transform, $\tilde{V}(u, v, w)$ is the 3D Fourier transform of $V(x, y, z)$, $w = \sqrt{(n_0/\lambda)^2 - u^2 - v^2}$, and (u_0, v_0, w_0) is the wave vector of the incident plane wave. A geometric interpretation of Eq. (2) is that the 2D Fourier transform of a scattered light field provides the 3D Fourier transform of $V(x, y, z)$ at the spatial frequency points on the Ewald's sphere, which is shown as a hemispherical cap in Fig. 2(b). The Ewald's sphere has a radius of n_0/λ and its center is shifted from the origin of the coordinates by $(-u_0, -v_0, -w_0)$; thus, the arrow in Fig. 2(b) represents the wave vector of the incident plane wave.

The scattered light field $U^{(S)}(x, y; u_0, v_0)$ in Eq. (2) is related to $U(x, y; u_0, v_0)$ as follows:

$$U^{(S)}(x, y; u_0, v_0) = U(x, y; u_0, v_0) - U^{(I)}(x, y; u_0, v_0), \quad (3a)$$

$$U^{(S)}(x, y; u_0, v_0) = U^{(I)}(x, y; u_0, v_0) \times \ln \left\{ \frac{U(x, y; u_0, v_0)}{U^{(I)}(x, y; u_0, v_0)} \right\}, \quad (3b)$$

where Eq. (3a) is used under the first-order Born approximation [40] and Eq. (3b) is used under the first-order Rytov approximation [42]. $U(x, y; u_0, v_0)$ is the light field obtained from the amplitude $A(x, y)$ and phase $\Phi(x, y)$ images, as shown in Figs. 2(a)(iii) and 2(a)(iv), respectively. $U^I(x, y; u_0, v_0)$ is the light field similarly obtained from the amplitude and phase images for an empty region. Here, we choose the first-order Rytov approximation, as it is more suitable for biological specimens [41]. In SHOT, the incident wave vector is determined by the two indices (i, j) shown in Fig. 2(a)(i) as well as design parameters such as the focal length of the condenser lens and the MLA pitch.

By mapping the light fields for different (u_0, v_0, w_0) values, we can determine the 3D spatial-frequency components of the sample at sufficiently many points to allow for reconstructing the 3D scattering potential and thus the

3D refractive-index map. The gray donut-shaped region in Fig. 2(b) represents the volume that can be retrieved using DHT, adopting dual-axis beam scanning; it is the support of the 3D optical transfer function (3D OTF) for DHT. SHOT uses a 2D array of lenslets, which generates the illumination beams tilted along two axes; thus, the 3D OTF of SHOT has a similar support, although the sampled data points are more sparsely distributed due to the smaller number of projection images. Applying the 3D inverse Fourier transform to the 3D spatial-frequency spectrum, we can obtain the 3D scattering potential of the sample, which can be converted to the 3D refractive-index map. Figure 2(c) shows horizontal cross sections of the 3D refractive-index map reconstructed from the raw image in Fig. 2(a) using the process described above.

Tomographic reconstruction from a finite number of projection images is an ill-posed inverse problem, as the illumination angle can be varied only within a limited angular range due to the finite numerical aperture of lenses. This insufficient data collection is responsible for the empty region, called the missing cone, near the origin of the coordinates in Fig. 2(b). The missing cone, which also appears in the 3D OTF of wide-field fluorescence microscopy [43,44], generates artifacts in the reconstructed tomogram. The missing-cone artifacts include the elongation of the reconstructed tomogram along the optical-axis direction and the underestimation of the refractive-index value or the fluorescence intensity. These problems can be alleviated using regularization incorporating additional information about the imaged specimen; for example, the 3D PSF [45]. Here, we use the non-negativity constraint [25], which is based on the fact that the refractive index of cells is always greater than that of the surrounding culture medium. This is not really an assumption, because the refractive index is known to increase with the density of the nonaqueous content (i.e., the dry mass) [46] and the cells are densely packed with proteins, nucleic acids, etc. The non-negativity constraint can be applied separately to the real and imaginary parts of the refractive index. When applied to the imaginary part, the non-negativity constraint means that there is no amplification of light, which can be justified for unmodified biological specimens. Here, we assume that there is no absorption by polystyrene beads or HeLa cells. A more detailed description of the reconstruction algorithm and a regularization technique to mitigate the missing-cone artifacts are referred to in our previous work [47]. Other alternative methods are available, which partially overcome the problem by recording reflection images [24], rotating the sample instead of scanning the illumination beam [26], or combining the sample rotation and illumination rotation [27,28].

Figure 3 shows example raw interferogram images for three wavelengths (550, 600, and 650 nm). For each image, one of the subimages is magnified and shown below and

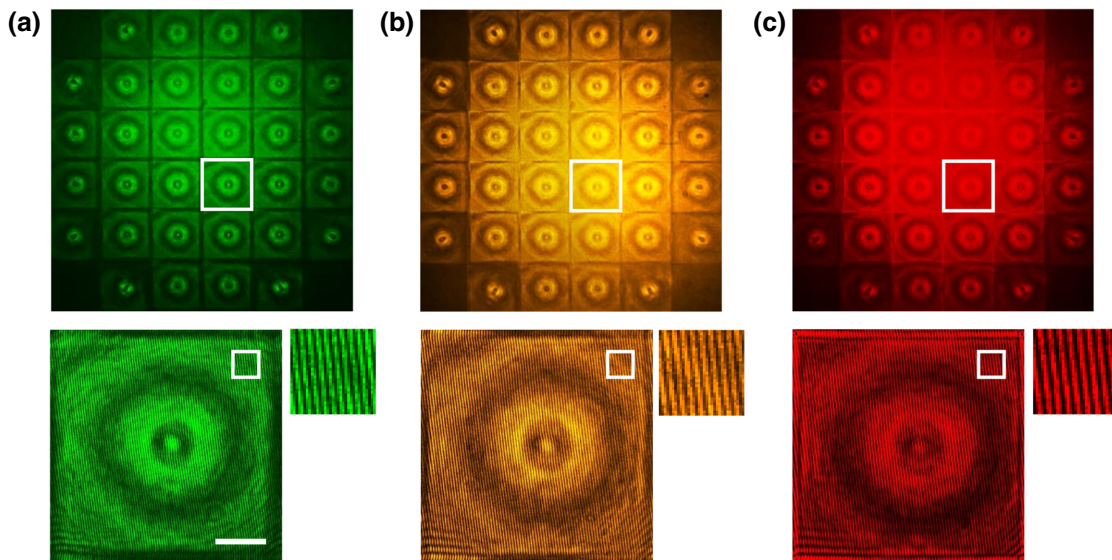


FIG. 3. Example raw images for different wavelengths: (a) 550 nm, (b) 600 nm, and (c) 650 nm. The raw images are pseudocolored based on the illumination wavelengths. For each image, a subimage is magnified and shown below; a square region in the background is further magnified and shown on the right. Although the coherence length of the laser light after the tunable filter is very short, owing to the VOPL strategy, the interference fringes show strong contrast for all the wavelength images, including the ones shown here. The fringe visibility is 0.43, 0.30, and 0.52 for the magnified background regions in (a), (b), and (c), respectively. Scale bar $10 \mu\text{m}$.

a background region is further magnified and shown on the right. Even though the coherence length of the filtered quasimonochromatic laser light is only about $20 \mu\text{m}$, the VOPL strategy allows us to record the projection images with high fringe visibility. This high fringe visibility is critical for accurate retrieval of the phase and thus for accurate measurement of the refractive index. Each projection image is circumscribed by the edge of lenslet, which forms sharp boundaries with the neighboring projection images. As the wavelength is varied for hyperspectral imaging, the boundary gets blurred, as shown in Fig. 3, this being due to chromatic aberration. We use a semiautomated code to select the inner region of each subimage for each wavelength. Any remaining edge diffraction in the selected region would contaminate the retrieved amplitude and phase images, and thus the reconstructed tomogram. Note that the cell in Fig. 3(c) for 650 nm is more defocused and is shown slightly larger than that in Fig. 3(a) for 550 nm, because the diffraction angle increases with the wavelength.

III. RESULTS AND DISCUSSION

To demonstrate hyperspectral 3D refractive-index imaging using the developed system, we measure the refractive index of $10\text{-}\mu\text{m}$ polystyrene beads (Polysciences, 17136-5) with the refractive-index dispersion well known from the literature [48]. The sample is immersed in index-matching oil (Cargille Laboratories, $n = 1.56$ at 589.3 nm and 25°C), the refractive-index values of which at the

measured wavelengths are obtained from the manufacturer. Figure 4(a) shows a bright-field image and center cross sections of the reconstructed tomograms at three selected wavelengths (550, 600, and 650 nm). The spatial resolution of SHOT is about $2 \mu\text{m}$; thus, the boundary of the bead is shown slightly blurred. The mean refractive index in the center cross section matches well with the refractive index of bulk polystyrene over the entire wavelength range, as shown in Fig. 4(b). The measurements of two polystyrene beads provide almost the same refractive-index value for each wavelength. The small deviation from the bulk polystyrene may be explained by the different crosslinking conditions.

Next, we measure the refractive index of HeLa cells in the same wavelength range (530–670 nm). Figure 5(a) shows a bright-field image and center cross sections of the reconstructed tomograms at the selected wavelengths (550, 600, and 650 nm). Note that the internal organelles can barely be seen in the single projection image [Fig. 2(a)(iv)]; however, they can be clearly seen in the cross sections of the reconstructed tomograms [Fig. 5(a)]. Bright-field imaging can directly record the cross-section image owing to the small depth of field; however, it does not provide the refractive-index value. The refractive index of the cell decreases as the wavelength increases, which is to be expected, as most biological cells, including HeLa cells, do not show anomalous dispersion in the visible range. Figure 5(b) shows the refractive-index values for the nucleus, cytoplasm, and nucleolus of three living HeLa cells in the wavelength range from 530 nm to

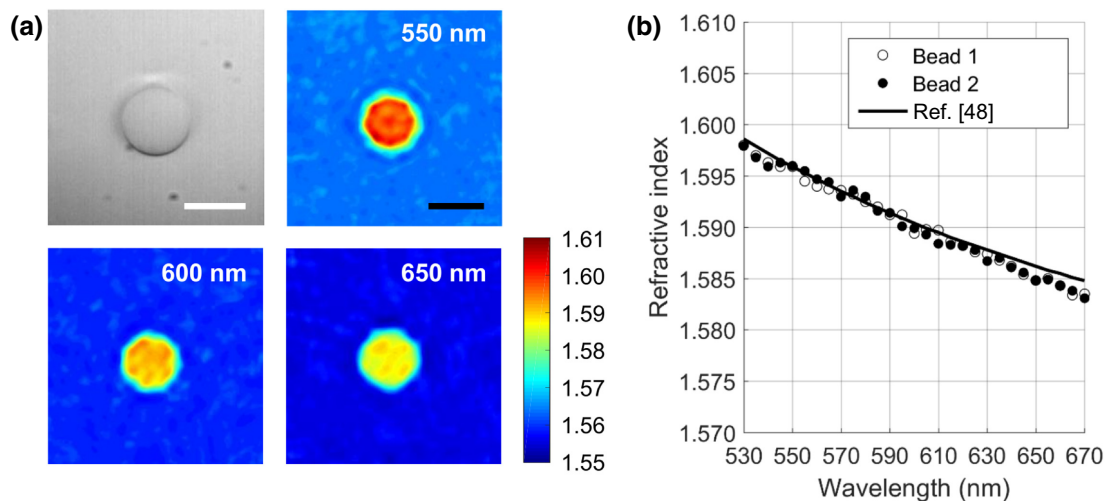


FIG. 4. The refractive-index dispersion of polystyrene beads in the (530–670)-nm wavelength range. (a) A bright-field image and the center cross sections of the reconstructed tomograms for 550, 600, and 650 nm. Scale bar $10\ \mu\text{m}$. (b) The refractive-index values for two polystyrene beads and the value for bulk polystyrene.

670 nm. The standard deviation is shown as an error bar at each wavelength. To automatically identify the organelles in each image, an image-segmentation algorithm using a fuzzy *c*-means (FCM) clustering algorithm is applied after refractive-index thresholding [49]. The FCM algorithm segments an image by grouping similar data points in the feature space (i.e., the refractive-index value in this work) into clusters [50]. Using bright-field images, which are acquired in parallel, we check the segmentation result manually, which confirms the validity of the automatic segmentation. The measured refractive-index values are slightly lower than, but concur with, those previously

obtained using 2D imaging [51], light scattering [52] (both applied to isolated nuclei), and 3D imaging at a single wavelength [25]. The slight difference may be attributed to biological variation, residual missing-cone artifact, or both. It is noteworthy that the missing-cone artifact would globally lower the refractive index; however, the shape of the dispersion curve would not be affected. As shown in Fig. 5(b), the refractive-index values for both the cytoplasm and nucleolus are higher than that for the nucleus (apart from the nucleolus) by about 0.008 for all measured wavelengths. Although the refractive index decreases by only 0.005 as the wavelength increases from 530 nm to

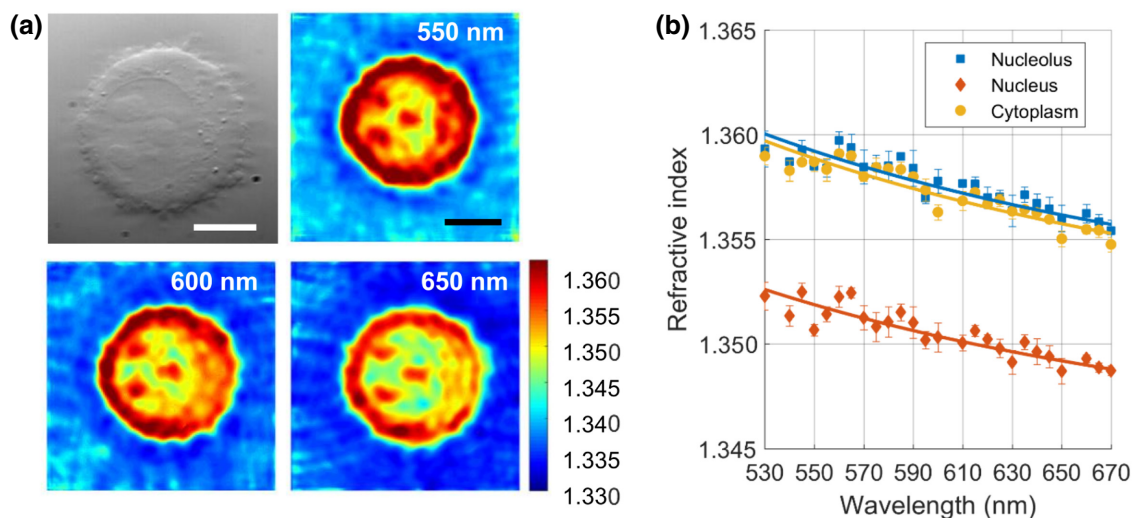


FIG. 5. The refractive-index dispersion of HeLa cells in the (530–670)-nm wavelength range. (a) A bright-field image and the center cross sections of the reconstructed tomograms for 550, 600, and 650 nm. Scale bar $10\ \mu\text{m}$. (b) The refractive-index values for nucleolus, nucleus, and cytoplasm within living HeLa cells. Each point represents the average of three samples and the error bar represents the standard deviation.

670 nm, the refractive-index values for each organelle are well fitted to Cauchy's equation with an adjusted R^2 value of about 0.8 or higher.

For particles of known size and regular shape (e.g., a sphere), a light-scattering measurement, in combination with Mie simulation, can be used to determine the refractive index [53]. For particles of irregular shape or heterogeneous across the volume, DHT is necessary. DHT is typically slow due to the need to acquire a series of projection images for varying illumination directions. Here, we use SHOT, a snapshot optical tomography technique that allows for simultaneous recording of all the projection images. Combining SHOT with a wavelength-scanning laser, we demonstrate hyperspectral 3D refractive-index imaging at high throughput. The measured refractive-index values for transparent polystyrene beads and cells match well with the dispersion of bulk polystyrene and previously reported values, respectively.

We have recently demonstrated hyperspectral 3D fluorescence imaging using snapshot projection optical tomography (SPOT) [54]. The technique has been extended to hyperspectral 3D absorption imaging by adding an illumination module [55]. For those demonstrations, we have combined SPOT with Fourier transform spectroscopy (FTS), which can provide high spectral resolution and a high signal-to-noise ratio. In this work, we demonstrate hyperspectral 3D refractive-index imaging using SHOT, because the existing snapshot optical tomography methods including SPOT are not compatible with coherent illumination. For hyperspectral 3D refractive-index imaging, here we use a broadband laser in combination with a tunable filter. The quasimonochromatic light has a sufficiently narrow bandwidth but the coherence length is still only about $20\ \mu\text{m}$. The chromatic aberration of the lenses can easily generate an optical path difference greater than the coherence length. Using a VOPL strategy, which varies the optical path length of the reference arm as the wavelength is scanned, we are able to achieve high fringe contrast over a broad wavelength range. Alternatively, common-path interferometry can be used to record the sample-induced phase alteration of the quasimonochromatic light [56]. We also note that, for near-infrared applications, a swept source can be used instead of the broadband laser and tunable filter. The swept source typically used for optical coherence tomography allows for a fast wavelength scan over a narrow wavelength range.

By adopting off-axis Fresnel holography and dividing the sensor array to record all the projection images, the spatial resolution of SHOT is currently limited to about $2\ \mu\text{m}$ in the transverse direction and $2.8\ \mu\text{m}$ along the vertical direction [31]. The spatial resolution can be further improved by reducing the number of projection images that are recorded simultaneously; however, this will lower the angular sampling and thus the quality of the 3D reconstruction. The optimal number of projection images to be

recorded would depend on the sample type. A calibration sample of a known shape and refractive index similar to those of the imaged specimen will help to optimize the imaging parameters [57]. The wavelength range can be extended by adopting optical components with higher transmission efficiency and active chromatic aberration compensation. It currently takes 41 s to acquire a four-dimensional (4D) data set (i.e., 2D projection images for 32 angles and 29 wavelengths) with the speed mainly limited by the motorized stage installed for the VOPL strategy and the camera frame rate. The data acquisition speed can be significantly improved using a translation stage with a faster response and a shorter settling time, a fast camera, or a fast tunable filter. On a desktop computer with a six-core 3.5-GHz CPU (Intel Core i7-5930K) and 32 GB of memory, the data processing takes about 10 min, with the regularization being the most time-consuming part. Parallel processing using a general-purpose graphic processing unit can greatly expedite the process [29].

IV. CONCLUSIONS

We demonstrate 4D (3D structural and one-dimensional spectral) refractive-index imaging using SHOT in combination with a wavelength-scanning laser and a variable optical path-length strategy. The hyperspectral 3D imaging system is demonstrated by measuring the optical dispersion of polystyrene microspheres and HeLa cells. The measured spectra matches previously published data that are obtained with different methods. With the high throughput, the developed system can be used to measure the refractive-index dispersions of a variety of microscopic particles and single living cells.

ACKNOWLEDGMENTS

This research was funded by the Research Growth Initiative of the University of Wisconsin-Milwaukee and the National Science Foundation (Grant No. 1808331).

-
- [1] R. Xu, Light scattering: A review of particle characterization applications, *Particuology* **18**, 11 (2015).
 - [2] R. Barer, K. F. A. Ross, and S. Tkaczyk, Refractometry of living cells, *Nature* **171**, 720 (1953).
 - [3] G. Popescu, Y. Park, N. Lue, C. Best-Popescu, L. Deflores, R. R. Dasari, M. S. Feld, and K. Badizadegan, Optical imaging of cell mass and growth dynamics, *Am. J. Physiol.* **295**, C538 (2008).
 - [4] Y. Sung, A. Tzur, S. Oh, W. Choi, V. Li, R. R. Dasari, Z. Yaqoob, and M. W. Kirschner, Size homeostasis in adherent cells studied by synthetic phase microscopy, *Proc. Natl. Acad. Sci. USA* **110**, 16687 (2013).
 - [5] K. L. Cooper, S. Oh, Y. Sung, R. R. Dasari, M. W. Kirschner, and C. J. Tabin, Multiple phases of chondrocyte

- enlargement underlie differences in skeletal proportions, *Nature* **495**, 375 (2013).
- [6] Y. Park, M. Diez-Silva, G. Popescu, G. Lykotrafitis, W. Choi, M. S. Feld, and S. Suresh, Refractive index maps and membrane dynamics of human red blood cells parasitized by *Plasmodium falciparum*, *Proc. Natl. Acad. Sci. USA* **105**, 13730 (2008).
- [7] R. Chandramohanadas, Y. Park, L. Lui, A. Li, D. Quinn, K. Liew, M. Diez-Silva, Y. Sung, M. Dao, and C. T. Lim, Biophysics of malarial parasite exit from infected erythrocytes, *PLoS One* **6**, e20869 (2011).
- [8] K. G. Phillips, C. R. Velasco, J. Li, A. Kolatkar, M. Luttgen, K. Bethel, B. Duggan, P. Kuhn, and O. J. T. McCarty, Optical quantification of cellular mass, volume, and density of circulating tumor cells identified in an ovarian cancer patient, *Front. Oncol.* **2**, 72 (2012).
- [9] K. G. Phillips, A. Kolatkar, K. J. Rees, R. Rigg, D. Marrinucci, M. Luttgen, K. Bethel, P. Kuhn, and O. J. McCarty, Quantification of cellular volume and sub-cellular density fluctuations: Comparison of normal peripheral blood cells and circulating tumor cells identified in a breast cancer patient, *Front. Oncol.* **2**, 96 (2012).
- [10] Z. Wang, G. Popescu, K. V. Tangella, and A. Balla, Tissue refractive index as marker of disease, *J. Biomed. Opt.* **16**, 116017 (2011).
- [11] K. J. Chalut, A. E. Ekpenyong, W. L. Clegg, I. C. Melhuish, and J. Guck, Quantifying cellular differentiation by physical phenotype using digital holographic microscopy, *Integr. Biol.* **4**, 280 (2012).
- [12] A. Wax, M. G. Giacomelli, T. E. Matthews, M. T. Rinehart, F. E. Robles, and Y. Zhu, Optical spectroscopy of biological cells, *Adv. Opt. Photonics* **4**, 322 (2012).
- [13] C. Yang, A. Wax, I. Georgakoudi, E. B. Hanlon, K. Badizadegan, R. R. Dasari, and M. S. Feld, Interferometric phase-dispersion microscopy, *Opt. Lett.* **25**, 1526 (2000).
- [14] Y. Park, T. Yamauchi, W. Choi, R. Dasari, and M. S. Feld, Spectroscopic phase microscopy for quantifying hemoglobin concentrations in intact red blood cells, *Opt. Lett.* **34**, 3668 (2009).
- [15] D. Fu, W. Choi, Y. Sung, Z. Yaqoob, R. R. Dasari, and M. Feld, Quantitative dispersion microscopy, *Biomed. Opt. Express* **1**, 347 (2010).
- [16] J. R. Weber, A. J. Durkin, B. J. Tromberg, D. J. Cuccia, W. R. Johnson, D. W. Wilson, G. H. Bearman, M. Hsu, A. Lin, and D. K. Binder, Multispectral imaging of tissue absorption and scattering using spatial frequency domain imaging and a computed-tomography imaging spectrometer, *J. Biomed. Opt.* **16**, 011015 (2011).
- [17] M. Torabzadeh, P. A. Stockton, G. T. Kennedy, R. B. Saager, A. J. Durkin, R. A. Bartels, and B. J. Tromberg, Hyperspectral imaging in the spatial frequency domain with a supercontinuum source, *J. Biomed. Opt.* **24**, 071614 (2019).
- [18] N. Verrier, M. Debailleul, and O. Haeberle, Recent progress in tomographic diffractive microscopy, *Proc. SPIE* **11351**, 1135104 (2020).
- [19] V. Balasubramani, A. Kuś, H.-Y. Tu, C.-J. Cheng, M. Baczevska, W. Krauze, and M. Kujawińska, Holographic tomography: Techniques and biomedical applications, *Appl. Opt.* **60**, B65 (2021).
- [20] Y. Sung, W. Choi, N. Lue, R. R. Dasari, and Z. Yaqoob, Stain-free quantification of chromosomes in live cells using regularized tomographic phase microscopy, *PLoS One* **7**, e49502 (2012).
- [21] C. Zuo, J. Sun, J. Zhang, Y. Hu, and Q. Chen, Lensless phase microscopy and diffraction tomography with multi-angle and multi-wavelength illuminations using a LED matrix, *Opt. Express* **23**, 14314 (2015).
- [22] J. Jung, K. Kim, J. Yoon, and Y. Park, Hyperspectral optical diffraction tomography, *Opt. Express* **24**, 2006 (2016).
- [23] Y. Sung, Spectroscopic Microtomography in the Visible Wavelength Range, *Phys. Rev. Appl.* **10**, 054041 (2018).
- [24] V. Lauer, New approach to optical diffraction tomography yielding a vector equation of diffraction tomography and a novel tomographic microscope, *J. Microsc.* **205**, 165 (2002).
- [25] W. Choi, C. Fang-Yen, K. Badizadegan, S. Oh, N. Lue, R. R. Dasari, and M. S. Feld, Tomographic phase microscopy, *Nat. Methods* **4**, 717 (2007).
- [26] F. Charriere, A. Marian, F. Montfort, J. Kuehn, T. Colomb, E. Cuche, P. Marquet, and C. Depeursinge, Cell refractive index tomography by digital holographic microscopy, *Opt. Lett.* **31**, 178 (2006).
- [27] S. Vertu, J. Flugge, J.-J. Delaunay, and O. Haeberle, Improved and isotropic resolution in tomographic diffractive microscopy combining sample and illumination rotation, *Cent. Eur. J. Phys.* **9**, 969 (2011).
- [28] B. Simon, M. Debailleul, M. Houkal, C. Ecoffet, J. Bailleul, J. Lambert, A. Spangenberg, H. Liu, O. Soppera, and O. Haeberle, Tomographic diffractive microscopy with isotropic resolution, *Optica* **4**, 460 (2017).
- [29] G. Dardikman, M. Habaza, L. Waller, and N. T. Shaked, Video-rate processing in tomographic phase microscopy of biological cells using CUDA, *Opt. Express* **24**, 11839 (2016).
- [30] J. Bailleul, B. Simon, M. Debailleul, L. Foucault, N. Verrier, and O. Haeberle, Tomographic diffractive microscopy: Towards high-resolution 3-D real-time data acquisition, image reconstruction and display of unlabeled samples, *Opt. Commun.* **422**, 28 (2018).
- [31] Y. Sung, Snapshot Holographic Optical Tomography, *Phys. Rev. Appl.* **11**, 014039 (2019).
- [32] S. K. Mirsky, I. Barnea, and N. T. Shaked, Dynamic tomographic phase microscopy by double six-pack holography, *ACS Photonics* **9**, 1295 (2022).
- [33] B. Xiong, X. Li, Y. Zhou, L. Wang, J. Wu, and Q. Dai, Snapshot Partially Coherent Diffraction Tomography, *Phys. Rev. Appl.* **15**, 044048 (2021).
- [34] J. W. Goodman, *Introduction to Fourier Optics* (Roberts & Company Publishers, Greenwood Village, Colorado, 2004).
- [35] K. Creath, in *Progress in Optics*, Vol. 26 (Elsevier, North-Holland, The Netherlands, 1988), p. 349.
- [36] B. C. Plattand and R. Shack, History and principles of Shack-Hartmann wavefront sensing, *J. Refract. Surg.* **17**, S573 (2001).
- [37] N. Streibl, Phase imaging by the transport equation of intensity, *Opt. Commun.* **49**, 6 (1984).
- [38] M. R. Teague, Deterministic phase retrieval: A Green's function solution, *J. Opt. Soc. Am.* **73**, 1434 (1983).

- [39] S. B. Mehtaand and C. J. Sheppard, Quantitative phase-gradient imaging at high resolution with asymmetric illumination-based differential phase contrast, *Opt. Lett.* **34**, 1924 (2009).
- [40] E. Wolf, Three-dimensional structure determination of semi-transparent objects from holographic data, *Opt. Commun.* **1**, 153 (1969).
- [41] Y. Sung, W. Choi, C. Fang-Yen, K. Badizadegan, R. R. Dasari, and M. S. Feld, Optical diffraction tomography for high resolution live cell imaging, *Opt. Express* **17**, 266 (2009).
- [42] A. J. Devaney, Inverse-scattering theory within the Rytov approximation, *Opt. Lett.* **6**, 374 (1981).
- [43] C. J. R. Sheppard, M. Gu, Y. Kawata, and S. Kawata, Three-dimensional transfer functions for high-aperture systems, *J. Opt. Soc. Am. A* **11**, 593 (1994).
- [44] P. J. Shaw, in *Handbook of Biological Confocal Microscopy* (Springer, New York, 2006), p. 453.
- [45] P. Sarderand and A. Nehorai, Deconvolution methods for 3-D fluorescence microscopy images, *IEEE Signal Process. Mag.* **23**, 32 (2006).
- [46] R. Barerand and S. Tkaczyk, Refractive index of concentrated protein solutions, *Nature* **173**, 821 (1954).
- [47] Y. Sungand and R. R. Dasari, Deterministic regularization of three-dimensional optical diffraction tomography, *J. Opt. Soc. Am. A* **28**, 1554 (2011).
- [48] N. Sultanova, S. Kasarova, and I. Nikolov, Dispersion properties of optical polymers, *Acta Phys. Pol.* **116**, 585 (2009).
- [49] A. Semechko, Fast fuzzy c-means image segmentation (2022), (<https://github.com/AntonSemechko/Fast-Fuzzy-C-Means-Segmentation>), GitHub, Retrieved September 2, 2021.
- [50] J. C. Bezdek, *Pattern Recognition with Fuzzy Objective Function Algorithms* (Springer, New York, 1981).
- [51] M. Schurmann, J. Scholze, P. Muller, J. Guck, and C. J. Chan, Cell nuclei have lower refractive index and mass density than cytoplasm, *J. Biophotonics* **9**, 1068 (2016).
- [52] Z. A. Steelman, W. J. Eldridge, J. B. Weintraub, and A. Wax, Is the nuclear refractive index lower than cytoplasm? Validation of phase measurements and implications for light scattering technologies, *J. Biophotonics* **10**, 1714 (2017).
- [53] M. R. McGrory, M. D. King, and A. D. Ward, Using Mie scattering to determine the wavelength-dependent refractive index of polystyrene beads with changing temperature, *J. Phys. Chem.* **124**, 9617 (2020).
- [54] C. Juntunen, I. M. Woller, and Y. Sung, Hyperspectral three-dimensional fluorescence imaging using snapshot optical tomography, *Sensors* **21**, 3652 (2021).
- [55] C. Juntunen, A. R. Abramczyk, I. M. Woller, and Y. Sung, Hyperspectral Three-Dimensional Absorption Imaging Using Snapshot Optical Tomography, *Phys. Rev. Appl.* **18**, 034055 (2022).
- [56] S. Bianchi, F. Brasili, F. Saglimbeni, B. Cortese, and R. Di Leonardo, Optical diffraction tomography of 3D microstructures using a low coherence source, *Opt. Express* **30**, 22321 (2022).
- [57] M. Ziemczonok, A. Kus, P. Wasylczyk, and M. Kujawinska, 3D-printed biological cell phantom for testing 3D quantitative phase imaging systems, *Sci. Rep.* **9**, 1 (2019).

Correction: Equation (3b) contained a minor error and has been fixed.